

Communication

Directed synthesis of carbon nanotube arrays based on layered double hydroxides toward highly-efficient bifunctional oxygen electrocatalysis



Zhenhua Li, Mingfei Shao*, Qihui Yang, Yang Tang, Min Wei*, David G. Evans, Xue Duan

State Key Laboratory of Chemical Resource Engineering, Beijing University of Chemical Technology, Beijing 100029, China

ARTICLE INFO

Keywords:

Carbon nanotube array
Bifunctional oxygen electrocatalyst
Zn–air battery
Layered double hydroxide

ABSTRACT

The exploration of highly-efficient, low-cost bifunctional oxygen electrocatalysts for both oxygen reduction reaction (ORR) and oxygen evolution reactions (OER) is critical for renewable energy storage and conversion technologies (e.g., fuel cells and metal–air batteries). Here we report the design and fabrication of free-standing nitrogen-doped carbon nanotube (NCNT) arrays *via* a directed growth approach as a high-performance bifunctional oxygen electrocatalyst. By virtue of the unique hierarchical nanoarray structure, uniform N-doping and decreased charge-transfer resistance, the as-prepared NCNT array exhibits rather high activity and stability in both ORR and OER, even superior to the mono-functional commercial Pt/C (for ORR) and IrO₂ (for OER). A flexible, rechargeable all-solid-state zinc–air battery is successfully fabricated by using this self-supporting NCNT electrode as air-cathode, which gives excellent discharge-charge performance and mechanical stability.

1. Introduction

Oxygen reduction/evolution reactions (ORR/OER) have attracted considerable attention owing to the increasing demands for renewable energy resources, such as rechargeable metal–air batteries and regenerative fuel cells [1,2]. In past decades, enormous efforts have been focused on the development of ORR and OER catalysts to accelerate these sluggish processes [3–6]. However, a highly-efficient bifunctional catalyst toward ORR and OER simultaneously is still a challenge. For example, much progress has been achieved in Pt-based electrocatalysts for ORR and Ir (or Ru)-based ones for OER [7,8], but a good catalyst for ORR normally shows poor activity toward OER and *vice versa*. Therefore, it is highly desirable to develop affordable and efficient candidates with bifunctional capability toward these two oxygen-involved electrocatalytic processes.

Recently, carbon-based materials have been demonstrated with large potential as noble metal-free oxygen electrocatalysts due to their excellent properties including facile modification of electronic/geometric structure, superior electrical conductivity and good stability [9–16]. Among them, carbon nanotubes (CNTs) with heteroatom doping (e.g., N, B, P and S) are recognized as effective electrocatalysts for ORR/OER [17–20]. Although the structure and morphology of single CNTs can be controlled to a certain degree by traditional methods (e.g., electric arc discharge (EAD) or chemical vapor deposition (CVD)) [19,20], the construction of hierarchical, uniform CNTs-based architecture is rarely obtained. Recent efforts have demonstrated that 3D

porous carbons (e.g., graphene foam [21,22], CNTs sponge [23,24], carbon-based network [25,26]) can give largely enhanced electrochemical performance due to their increased surface area and abundant mesopores for mass transport. Therefore, how to achieve well-defined, highly-efficient CNTs electrocatalysts toward both ORR and OER *via* material design and synthesis exploration remains a big challenge.

Herein, we report the design and fabrication of a free-standing 3D nitrogen-doped carbon nanotube (NCNT) arrays *via* a directed growth approach: supported layered double hydroxides (LDHs) nanoplatelet catalyzes the *in situ* growth of NCNT array on its surface, with a metal–organic framework (MOF) compound serving as carbon and nitrogen source in the pyrolysis process. The as-synthesized material shows a hierarchical cactus-like morphology, consisting of well-distributed NCNTs (diameter: ~11 nm; length: several hundred nanometer; nitrogen content: 3%) vertically grafted on both sides of LDH-derived nanoplatelet. Interestingly, the 3D NCNT array electrode displays satisfactory activity and stability in both ORR and OER, even superior to the mono-functional oxygen electrocatalysts, such as commercial Pt/C (for ORR) and IrO₂ (for OER). As a proof of concept, a flexible, rechargeable all-solid-state Zn–air battery is fabricated by using the 3D NCNT array as air-cathode, giving rise to excellent discharge-charge performance (charge/discharge potential: 1.98 V/1.02 V at 5 mA cm⁻²; energy density: ~382 Wh kg⁻¹), which is attributed to the uniform N-doping (active sites) and hierarchical nanoarray structure (charge/mass transport channel). This work provides a facile approach for the fabrication of NCNT array toward highly-efficient bifunctional ORR/

* Corresponding authors.

E-mail addresses: shaomf@mail.buct.edu.cn (M. Shao), weimin@mail.buct.edu.cn (M. Wei).

OER electrocatalysis.

2. Experimental section

2.1. Synthesis of 3D NCNT array

2.1.1. Preparation of CoAl-LDH nanoplatelets array

The CoAl-LDH array was synthesized using a *in-situ* growth process on a Ni foam substrate. Typically, 1 mmol of $\text{Co}(\text{NO}_3)_2 \cdot 6\text{H}_2\text{O}$, 0.5 mmol of $\text{Al}(\text{NO}_3)_3 \cdot 9\text{H}_2\text{O}$, 5 mmol of NH_4F and 35 mmol of urea were dissolved in 50 mL of deionized H_2O , which was then poured into a Teflon-lined stainless steel autoclave. A piece of Ni foam ($30 \times 60 \times 0.1$ mm; pretreated with absolute ethanol, acetone and deionized water, each for 15 min) was immersed into the above solution, sealed, heated at 90 °C for 6 h. The substrate coated with CoAl-LDH nanoplatelets array was then withdrawn, washed thoroughly with H_2O and dried at 60 °C for 12 h.

2.1.2. Preparation of ZIF-67

ZIF-67 was synthesized in methanol at room temperature [22]. Typically, 50 mL of 2-methylimidazole (MeIM) methanol solution (0.8 M) was rapidly poured into 50 mL of $\text{Co}(\text{NO}_3)_2 \cdot 6\text{H}_2\text{O}$ methanol solution (0.1 M) with magnetic stirring at room temperature for 15 min. The product was collected by centrifugation (3000 rpm, 5 min) and washed several times by methanol.

2.1.3. Preparation of 3D NCNT array

The powdered sample of ZIF-67 (20 mg) was placed in a crucible, and a piece of Ni foam ($30 \times 30 \times 0.1$ mm) supported CoAl-LDH nanoplatelets array is installed horizontally over the crucible. A temperature-programmed furnace was used to perform the 3D NCNT array growth process under H_2 atmosphere at 800 °C for 2 h, and the heating rate was 5 °C min^{-1} .

2.2. Characterization

Shimadzu XRD-6000 diffractometer with a Cu K α source was used to measure the X-ray diffraction patterns of the samples (scan range: 3°–70°, scan step: 2° min^{-1}). Thermo VG ESCALAB 250 X-ray photoelectron spectrometer was used to perform the X-ray photoelectron spectra (XPS) of the samples with a pressure of about 2×10^{-9} Pa and using Al K α X-rays as the excitation source. Raman microspectrometer (Renishaw, inVia-Reflex, 532 nm) was used to carry out the Raman measurements with 532 nm of excitation by using a confocal. The pore size analysis was performed by Barrett-Joyner-Halenda (BJH) method, using a Quantachrome Autosorb-1CVP analyzer. The morphology investigation was using a Zeiss SUPRA 55 scanning electron microscope (SEM, with an accelerating voltage of 20 kV), which combine with energy dispersive X-ray spectroscopy (EDX). Transmission electron microscope (TEM) images were recorded using a Philips Tecnai 20 and JEOL JEM-2010 high-resolution transmission electron microscope with an accelerating voltage of 200 kV.

2.3. Electrochemical measurements

Electrochemical measurements were performed by using a CHI660E electrochemical workstation (Shanghai Chenhua Instrument Co., China) in 0.1 M KOH solution with a conventional three-electrode cell, in which the Ag/AgCl (3.5 M KCl) and platinum electrode were used as reference and counter electrode, respectively.

2.3.1. ORR measurements

For the ORR measurements, a rotating disk electrode (RDE) of 3.0 mm in diameter and rotating ring-disk electrode (RRDE) of 5.61 mm in diameter were used as the substrate for the working electrode. Prior to use, RDE and RRDE were polished by aqueous

alumina suspension on felt polishing pads, and washed with deionized water and ethanol. To prepare the working electrode, the NCNT array (2 mg) was firstly scraped from the Ni foam substrate, and then dispersed in a solution containing 780 μL of deionized water, 200 μL of ethanol and 20 μL of 5 wt% Nafion solution, followed by a strong ultrasonic treatment to form a uniform black ink. 7 μL of the catalyst ink was dripped onto the glassy carbon surface with a loading of 0.2 mg cm^{-2} for all samples including commercial Pt/C catalyst (20 wt % of Pt). Before test, a N_2 or O_2 flow was used for the electrolyte in the cell for 30 min to give a saturation state. The cyclic voltammetry (CV) experiments were performed in N_2 - and O_2 -saturated 0.1 M aqueous KOH electrolyte solution at a scan rate of 10 mV s^{-1} . RDE tests were measured in O_2 -saturated 0.1 M KOH at different speed rates (625, 900, 1225, 1600, 2025, 2500 rpm) with a sweep rate of 10 mV s^{-1} . RRDE measurements were also conducted in O_2 -saturated 0.1 M KOH at room temperature. The disk potential was cycled from -1 – 0.2 V at a scan rate of 5 mV s^{-1} and the ring potential was constant at 0.5 V. The stability tests were carried out at -0.464 V vs. Ag/AgCl in O_2 -saturated 0.1 M KOH ($\omega=1600$ rpm) by the chronoamperometric method. During the crossover tests, 2 M of methanol was added into O_2 -saturated 0.1 M KOH within ~ 200 s. The ORR measurement of the NCNT array/Ni foam electrode was operated in O_2 -saturated KOH solution (1 M) with continuous O_2 pump into solution.

2.3.2. OER measurements

The OER performances were evaluated by using Ni foam supported NCNT array (or CoAl-LDH array, CoAl-LDH-R) as working electrode.

2.4. Fabrication of Zn–air battery

2.4.1. Liquid Zn–air battery

The liquid Zn–air battery was tested in a home-built electrochemical cell. A two electrode configuration was assembled, which included Ni foam supported NCNT array as O_2 catalysis electrode and air diffusion layer, Zn foil as the anode and 6 M KOH+0.2 M zinc acetate as the electrolyte.

2.4.2. All-solid-state flexible Zn–air battery

The flexible/wearable all-solid-state Zn–air battery was fabricated by using Ni foam supported NCNT array as air-cathode, zinc foil (0.05 mm in thickness) as the anode, and alkaline poly(vinyl alcohol) (PVA) gel as the electrolyte. The gel polymer electrolyte was prepared as follow: polyvinyl alcohol (PVA, 5 g) was added into 0.1 M KOH (50 mL) solution containing 0.02 M zinc acetate at 90 °C with stirring, until the solution became uniform. Then, the solution was poured onto a glass plate to form a thin film, which was freeze-dried at -3 °C over 12 h and then thawed at room temperature. The procedure was repeated twice to gelate the PVA robustly. Finally, the as-prepared NCNT array and zinc foil were placed on the two sides of PVA gel, pressed with a high pressure to obtain the Zn–air battery.

2.4.3. Battery tests

The Zn–air battery was tested in ambient atmosphere. The polarization curve measurements were performed by LSV (5 mV s^{-1}) at 25 °C with CHI600e electrochemical working station. Both the current density and power density were normalized to the effective surface area of air electrode. The galvanostatic discharge and discharge-charge cycling were carried out by LAND testing system. The blue light-emitting diode (LED, 1.5 V) is commercial available.

3. Results and discussion

3.1. Structural and morphological characterization of 3D NCNT array

The preparation of 3D NCNT array is achieved by directed catalytic

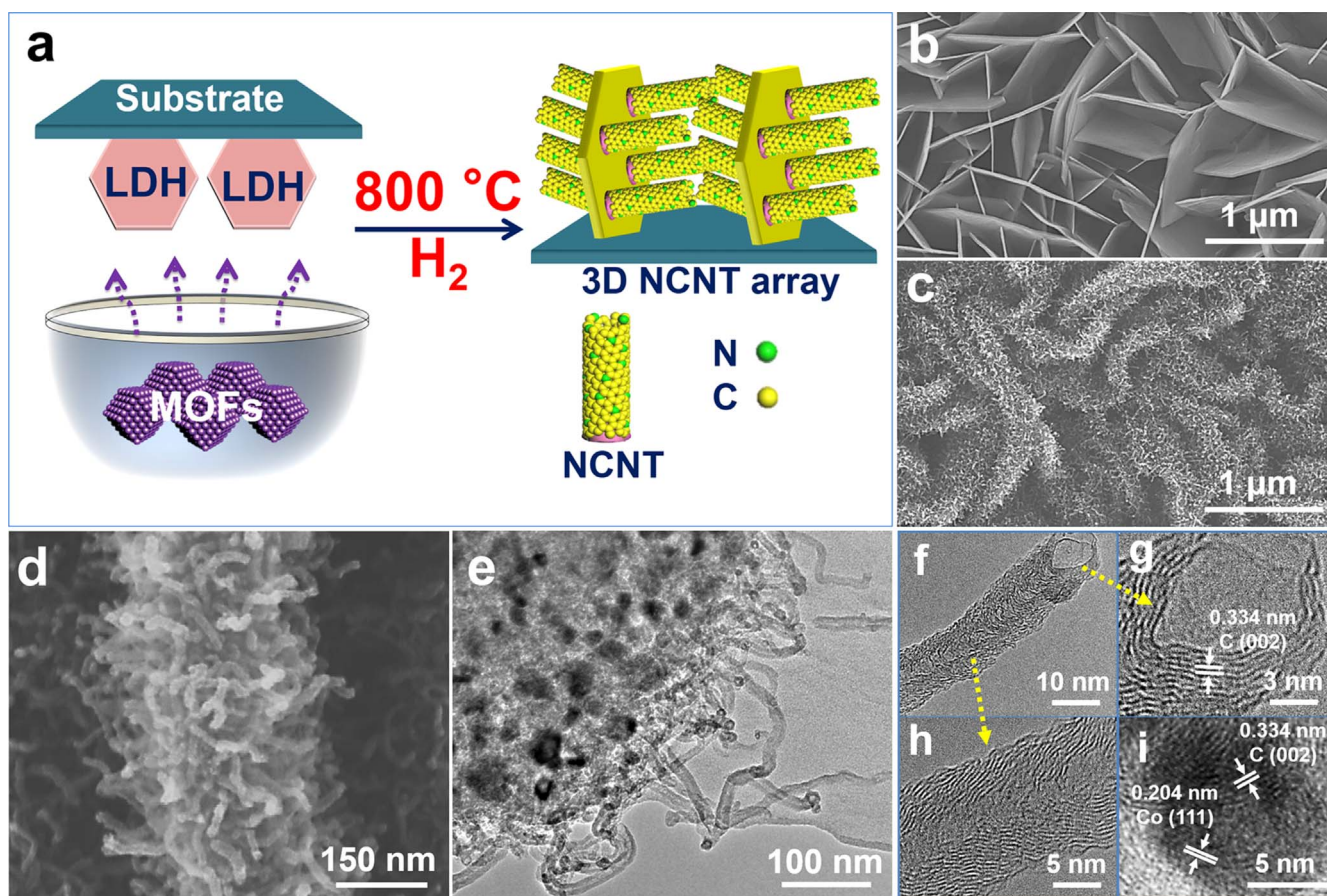


Fig. 1. The synthesis of 3D NCNT array. (a) Schematic illustration for the synthesis of 3D NCNT arrays by a facile directed growth process. SEM images of (b) CoAl-LDH nanosheets and (c,d) NCNT arrays on LDH nanosheets. (e) TEM image and (f-i) HRTEM images of the as-obtained NCNT.

growth of NCNT on supported CoAl-LDH nanosheets with a MOF compound as carbon and nitrogen source (Fig. 1a). In this process, a piece of Ni foam supported CoAl-LDH nanosheets is installed horizontally over a crucible which contains zeolitic imidazolate framework-67 (ZIF-67) (Fig. S1); after heating at 800 °C for 2 h in a H₂ atmosphere, uniform NCNT arrays are obtained on both sides of LDH-derived nanosheets. Herein, the escaped carbon and nitrogen species from ZIF-67 during the pyrolysis process serve as carbon and nitrogen source simultaneously, which is proved by TG-MS analysis (Fig. S2); while the supported CoAl-LDH nanosheet acts as catalyst for the growth of NCNT arrays. Fig. 1b displays top-view scanning electron microscopy (SEM) image of the as-prepared CoAl-LDH nanosheets grown on Ni foam substrate, from which uniform nanosheet arrays with a diameter of 1–2 μm and thickness of ~40 nm are observed. After the NCNT growth, SEM images show numerous worm-like nanotubes are immobilized on both sides of LDH-derived nanosheets with a thickness of ~300 nm (Figs. 1c,d; Fig. S3). Transmission electron microscopy (TEM) image further confirms the existence of CNT array shell on the surface of nanosheet (Fig. 1e). HR-TEM images of a single CNT (Fig. 1f,g) reveal a hollow and top opening structure with a uniform diameter of ~11 nm. The CNTs are crystallized with an interplanar lattice fringe of 0.334 nm, corresponding to the C (002) plane [27]. Notably, the graphitic layers in the CNT wall are not perfectly parallel to the axis direction, and abundant edges rather than basal plane are exposed on the surface of CNTs (Fig. 1h). It has been reported that this unique structure introduces abundant edges rather than basal plane exposed on the surface of CNTs, and would be beneficial to electrocatalytic properties [4]. In addition, some nanoparticles (diameter: ~12 nm) are observed at the bottom of CNTs (Figs. 1e,i and Fig. S4), with a lattice fringe of 0.204 nm, corresponding

to the (111) plane of metallic Co [28]. Co nanoparticles are produced *via* the high temperature reduction of CoAl-LDH precursor in a H₂ atmosphere, which could serve as the catalyst for the crystallization and growth of CNT [29].

Fig. 2a shows the X-ray diffraction (XRD) patterns of Ni foam substrate, supported CoAl-LDH nanosheets and the resulting NCNT arrays, respectively. The Ni foam substrate displays two strong reflections (2θ 44° and 51°) indexed to the (111) and (200) plane of a cubic metallic nickel. The sample of CoAl-LDH nanosheets shows a typical LDH phase with peaks at 11.7°, 23.5°, 34.8°, 39.2°, 46.8°, 59.7° and 60.9°, corresponding to the (003), (006), (012), (015), (018), (110) and (113) reflection of CoAl-LDH [30,31]. After the growth of NCNT array, the LDH phase disappears with a new reflection observed at ~26°, attributed to the C(002) plane. XRD pattern of the NCNT powdered sample scraped from the substrate is further measured: two peaks located at 44° and 51° are observed (Fig. S5), corresponding to the (111) and (200) crystal plane of crystal plane of metallic Co [26]. The metallic Co is formed through the structural transformation of CoAl-LDH, which is further proved by reducing pure CoAl-LDH array in H₂ atmosphere without carbon source (denoted as CoAl-LDH-R; Fig. S6). Raman spectrum of NCNT array also reveals the characteristic G band (1590 cm⁻¹) and D band (1330 cm⁻¹) for the graphitic carbon (Fig. 2b). The chemical composition of as-prepared NCNT was investigated by X-ray photoelectron spectroscopy (XPS). The full XPS spectrum of NCNT arrays shows element signals of C, O, N, Co and Al (Fig. 2c and Table S1), in approximately accordance with the results of EDX spectrum (Fig. S7). The high-resolution C 1s spectrum shows two signals at ~284.5 eV and ~285.6 eV, corresponding to the C–C, C=N and C=O, respectively (Fig. 2d). The O 1s spectrum (Fig. S8a) displays C=O signal, demonstrating the existence of surface-bound oxygen

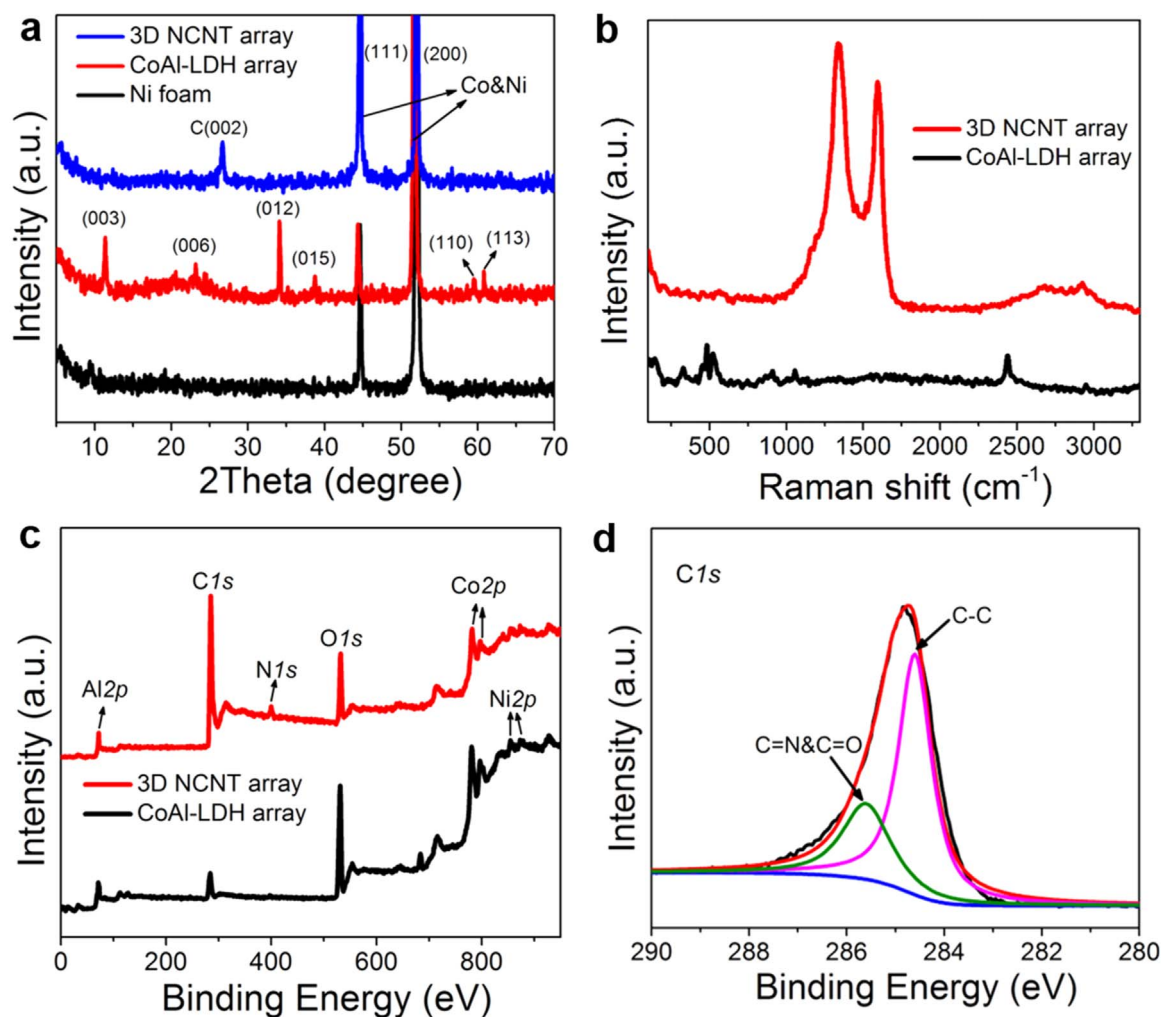


Fig. 2. Compositional and structural information of 3D NCNT array. (a) XRD patterns of Ni foam substrate, CoAl-LDH nanoplatelets and NCNT arrays, respectively. (b) Raman and (c) XPS spectra of the CoAl-LDH nanoplatelets and NCNT arrays, respectively. (d) High-resolution XPS spectra of C 1s for the NCNT arrays.

group. It has been reported that the C=O group on the surface of carbon acts as the real active site for OER [32]. The large amount of O is due to the presence of Al₂O₃ in the skeleton of 3D NCNT derived from CoAl-LDH precursor. The high-resolution N1s spectrum (Fig. S8b) reveals the presence of three nitrogen species: pyridinic-N (pyr-N, 398.3 eV), pyrrolic-N (pyrr-N, 400.2 eV), and graphitic-N (grap-N, 401.2 eV), which verifies the successful doping of N in the as-prepared CNT array. Moreover, the high resolution Co 2p XPS spectrum shows three types of Co species: metallic Co (778.5 eV), CoO_x or CoC_xN_y (780.5 eV) and CoN_z (782 eV) with a percentage of 49.3%, 28.2% and 22.5%, respectively (Fig. S8c). The results verify the presence of Co–N bond, which has been reported as one of the most efficient active sites for ORR.

The key role for the formation of NCNT arrays was studied. It is found that pure Ni foam substrate shows no catalytic behavior for the growth of NCNT (Fig. S9). For the sample of CoAl-LDH/Ni foam, in the absence of carbon source (ZIF-67), only reduced CoAl-LDH nanoplatelets (CoAl-LDH-R) are observed (Fig. 3b). Moreover, a replacement of H₂ by N₂ during the pyrolysis process cannot induce the formation of well-organized NCNT arrays (Fig. S10). The results indicate that there is a synergistic effect among CoAl-LDH, carbon source and H₂ for the catalytic growth of NCNTs. Time-dependent experiments were carried out to further understand the growth process of such NCNT array (Fig. 3a). In comparison with the sample without carbon source (CoAl-LDH-R, Fig. 3b), tiny CNT subunits appear on the surface of

nano-platelets with a short synthesis time (5 min, Fig. 3c), which grow longer gradually with a well-defined cactus-like morphology (1 h and 2 h, Fig. 3d,e). As the NCNT growth time is further prolonged, the whole surface of nano-platelet is covered with much denser and longer CNT (5 h and 10 h, Fig. 3f,g). It is worth mention that a similar result is also obtained by changing the amount of ZIF-67 with the same pyrolysis time for CNT growth (Fig. S11), indicating the length and density of NCNT array can be well-controlled by tuning the NCNT growth time or the amount of carbon source. Therefore, it can be concluded that CoAl-LDH array acts as a precursor to generate well-dispersed metallic Co nanoparticles in a reductive atmosphere, which catalyze the growth of NCNT array; ZIF-67 serves as carbon and nitrogen source simultaneously. Furthermore, well-defined NCNT array can also be obtained by using NiAl-LDH as the template and catalyst precursor (Fig. S12), illustrating the universality of this method.

3.2. Oxygen reduction reaction (ORR)

The ORR catalytic activities of the NCNT array and corresponding reference samples are investigated. Since the 3D NCNT array electrode cannot directly used for the RDE and RRDE study, we utilize the powder based sample that scraped from the Ni foam substrate to perform this measurement approximately, so as to obtain some information on the intrinsic activity of electrocatalyst. As shown in

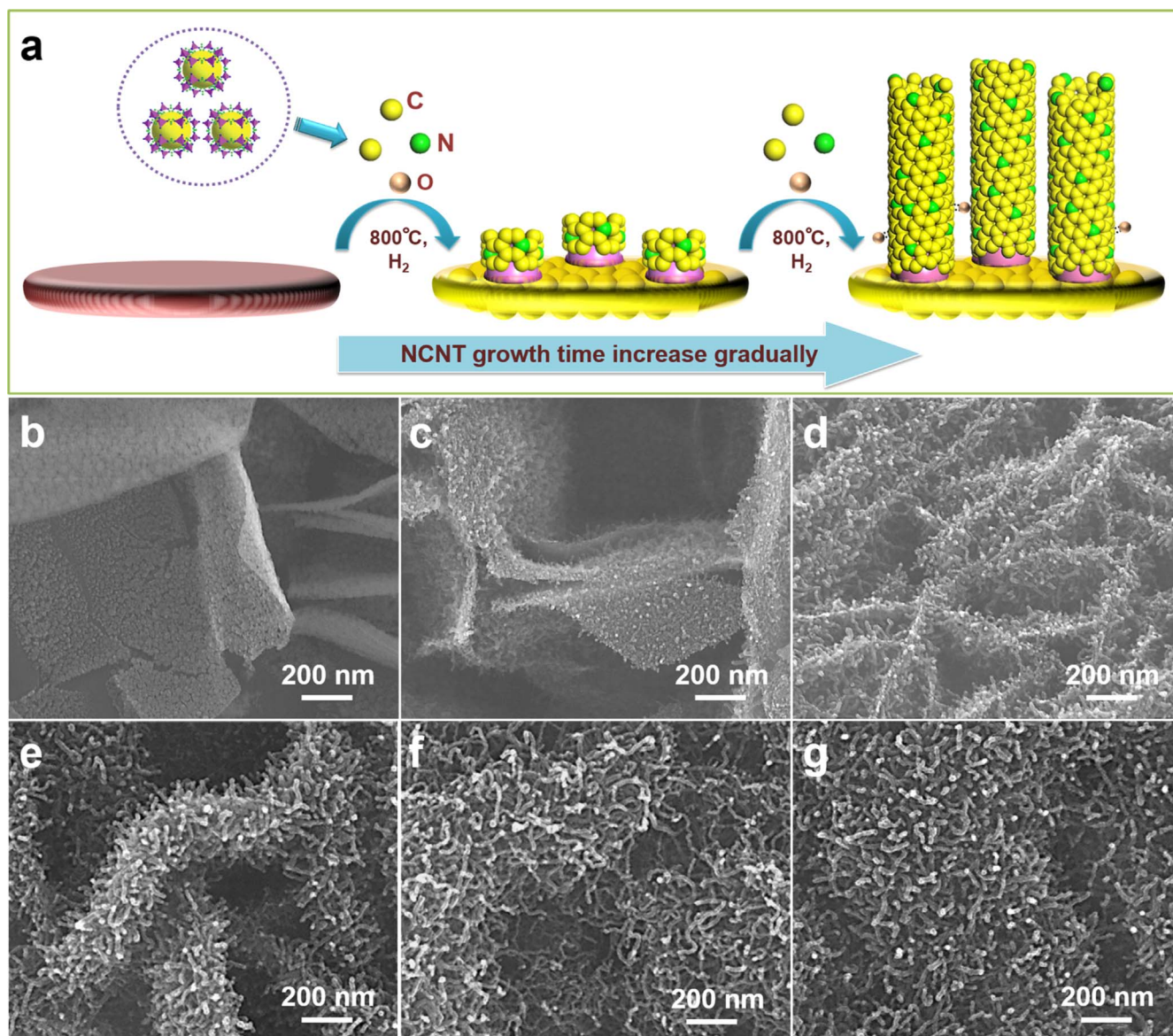


Fig. 3. Growth process of 3D NCNT array. (a) Schematic illustration for the growth process of the NCNT arrays along with the increase of NCNT growth time. SEM images of (b) CoAl-LDH-R, and the NCNT samples with prolonged pyrolysis time: (c) 5 min (d) 1 h, (e) 2 h, (f) 5 h, (g) 10 h.

Fig. 4a, the cyclic voltammetry (CV) curve of NCNT array shows obviously enhanced cathodic peak in O_2 -saturated alkaline solution (0.1 M KOH), predicting a superior ORR activity of this sample. Linear sweep voltammetry (LSV) studies show that the NCNT array exhibits a more positive onset potential of 0.925 V vs. RHE and half-wave potential of 0.812 V vs. RHE, in comparison with CoAl-LDH and CoAl-LDH-R (Fig. 4b); it also gives a larger diffusion-limited current density (5.45 mA cm^{-2}), indicating an excellent ORR activity. Tafel slopes of NCNT and Pt/C are obtained from the linear plots of LSVs at 1600 rpm (Fig. 4c), both of which show typical two-stage linear region at low overpotential (η_L) and high overpotential (η_H). The NCNT array presents a lower tafel slopes at both η_L (69 mV dec^{-1}) and η_H (118 mV dec^{-1}), which are less than those of the commercial Pt/C catalyst (76 mV dec^{-1} at η_L ; 135 mV dec^{-1} at η_H), suggesting the NCNT possesses a more efficient mass diffusion and a faster electron transfer rate. Rotating disk electrode (RDE) measurements at various rotating speeds are carried out to study the ORR electron-transfer process of NCNT array and the kinetic parameters are analysed by the Koutecky–Levich (K–L) equation (Fig. 4d). The linearity of K–L plots for NCNT indicates a similar electron transfer number (n) at various potentials

(Fig. S13) [33]. The calculated electron transfer number for NCNT array is ~ 4.0 within 0.2–0.7 V vs. RHE, close to the theoretical value of Pt/C catalyst and much larger than that of other reference catalysts (Fig. S14 and S15). Furthermore, the formation of HO_2^- during the ORR process is monitored by a rotation ring-disk electrode (RRDE) technique (Fig. S16). As shown in Fig. 4e, the NCNT exhibits a low HO_2^- yield ($< 10\%$) and a large electron transfer number (n) ranges in 3.75–3.96, consistent with the results of the RDE study. The stability of the NCNT array is evaluated by chronoamperometric (CA) and LSV measurements: no obvious negative shift in the LSV curve of NCNT array is observed after 20000 s of continuous CA operation (Fig. 4f), superior to that of Pt/C catalyst ($\sim 36 \text{ mV}$ negative shift in half-wave potential; Fig. S17). Furthermore, the stability test was performed within 105 h. As shown in the $I-t$ curve (Fig. S18a), the current density of NCNT maintains $\sim 99\%$ and 97.5% after 20 h and 50 h of continuous measurement, and still keeps $\sim 95\%$ after 105 h, demonstrating a satisfactory long-term stability of this carbon-based catalyst. Moreover, with the addition of 2 M methanol, neither the LSV curve (Fig. 4f) nor CA curve (Fig. S18b) for the NCNT sample display variation; in contrast, Pt/C catalyst suffers from a sharp loss in activity.

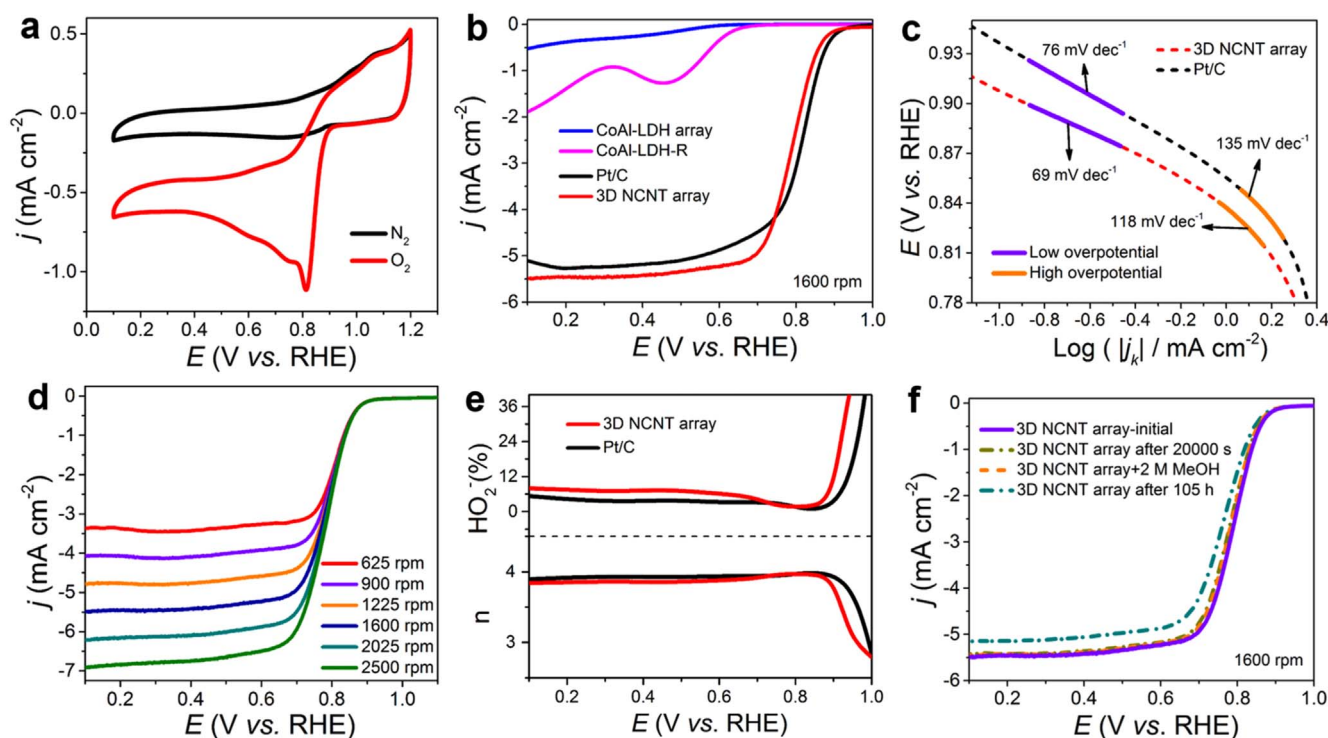


Fig. 4. Electrochemical oxygen reduction behavior over 3D NCNT array. (a) CV curves of NCNT in O_2 -saturated (red) and N_2 -saturated (black) 0.1 M KOH solution. (b) LSV curves (1600 rpm) of NCNT, CoAl-LDH-R, CoAl-LDH and commercial Pt/C catalyst. (c) Tafel slopes for NCNT and Pt/C catalyst. (d) LSV curves for NCNT at different rotation rates. (e) Peroxide yield and electron transfer number of NCNT and Pt/C catalyst at various potentials based on the RRDE measurement. (f) LSV curves of NCNT before and after 20000 s and 105 h of CA measurements, and the LSV curves of NCNT in O_2 -saturated 0.1 M KOH + 2 M CH_3OH solution.

This demonstrates that the NCNT catalyst possesses a stronger tolerance against crossover effect than Pt/C catalyst.

3.3. Oxygen evolution reaction (OER)

The OER activities of the NCNT array and reference samples were evaluated in 0.1 M KOH solution. As shown in Fig. 5a, the LSV curves display that the NCNT array possesses the lowest OER onset potential and the highest current density among all the samples, revealing the optimal OER activity. Fig. 5b gives the overpotential (η) of the catalysts at different current densities (10 and 50 $mA\ cm^{-2}$, denoted as $\eta_{j=10}$ and $\eta_{j=50}$, respectively). It can be seen that both $\eta_{j=10}$ (265 mV) and $\eta_{j=50}$ (368 mV) for the as-prepared NCNT array are much lower than those of CoAl-LDH array, CoAl-LDH-R and the reported commercial IrO_2 in the literature [3,38,42,43]. The Tafel slope of NCNT array is 69.5 $mV\ dec^{-1}$ (Fig. 5c), also smaller than that of CoAl-LDH array (128.1 $mV\ dec^{-1}$), CoAl-LDH-R (76.2 $mV\ dec^{-1}$), indicating its superior OER performance. This can be attributed to the higher electrochemical surface area (ECSA, Fig. S19), lower charge-transfer resistance (Fig. S20), and the unique hierarchical porous structure (with a wide pore-size distribution mainly centered at 2.2 and 12.5 nm; Fig. S21) for the 3D NCNT array. Moreover, the 3D NCNT array shows a faradaic efficiency of $\sim 100\%$ after a chronopotentiometry (CP) measurement with constant current of 100 $mA\ cm^{-2}$ for 10 min (Fig. S22), indicating a satisfactory energy conversion efficiency from electric energy to chemical energy. A durability test was carried out by CP measurement at 50 $mA\ cm^{-2}$ (Fig. 5d). The operating overpotential for the NCNT array is nearly constant after 20 h of testing and the electrode surface maintains its original cactus-like architecture (Fig. 5d, inset).

The overall oxygen electrode activity is studied by the potential gap (ΔE) between the ORR ($E_{1/2}$, half-wave potential) and the OER ($E_{j=10}$, potential required at an current density of 10 $mA\ cm^{-2}$) [13]. Since it's

hard to study the value of $E_{1/2}$ for the NCNT array/Ni foam sample, herein, the $E_{1/2}$ and $E_{j=10}$ of NCNT array were obtained by scraping the NCNT from Ni foam and coating on glass carbon (GC) electrode. The GC electrode supported NCNT exhibits an $E_{1/2}$ of 0.81 V vs. RHE and $E_{j=10}$ of 1.65 V vs. RHE ($\Delta E = 0.84$ V), which is among the highest level of carbon-based bifunctional catalysts reported recently (Fig. 5e and Table 1). In comparison with the GC electrode supported NCNT, Ni foam supported NCNT array shows significantly enhanced electrocatalytic performances for both OER and ORR. This can be ascribed to the hierarchical nanostructure of this self-supported 3D NCNT electrode, which promotes the structural feature of each component with sufficient exposure of active sites and fast ion/electron transport, and hence realizes the full potential of this composite material. Moreover, a repeated switch between ORR and OER based on the chronoamperometric measurement was performed for the stability test. As shown in $I-t$ curves of 3D NCNT array (Fig. S23a), no obvious performance decay is observed after 10 times of switch between ORR and OER; and the electrode surface maintains its original cactus-like architecture (Fig. S23b), further demonstrating a superb stability of the bifunctional NCNT array catalyst.

3.4. Zn-air battery

Both the ORR and OER are essential steps in the metal-air batteries [34,35]. To identify the practicality in metal-air batteries of this 3D NCNT array, a homemade primary Zn-air battery device was constructed with zinc plate as the anode, NCNT array/Ni foam as the cathode, and 6.0 M KOH+0.2 M zinc acetate aqueous solution as the electrolyte. Fig. 6a presents the polarization and power density curves for the as-fabricated liquid Zn-air battery. The device displays an open circuit voltage of 1.47 V (Fig. S24), a current density of $\sim 160\ mA\ cm^{-2}$ at 1.0 V and a peak power density of 190 $mW\ cm^{-2}$ at 0.70 V, which are higher than most reported Zn-air primary batteries (Table S2). Fig. 6b

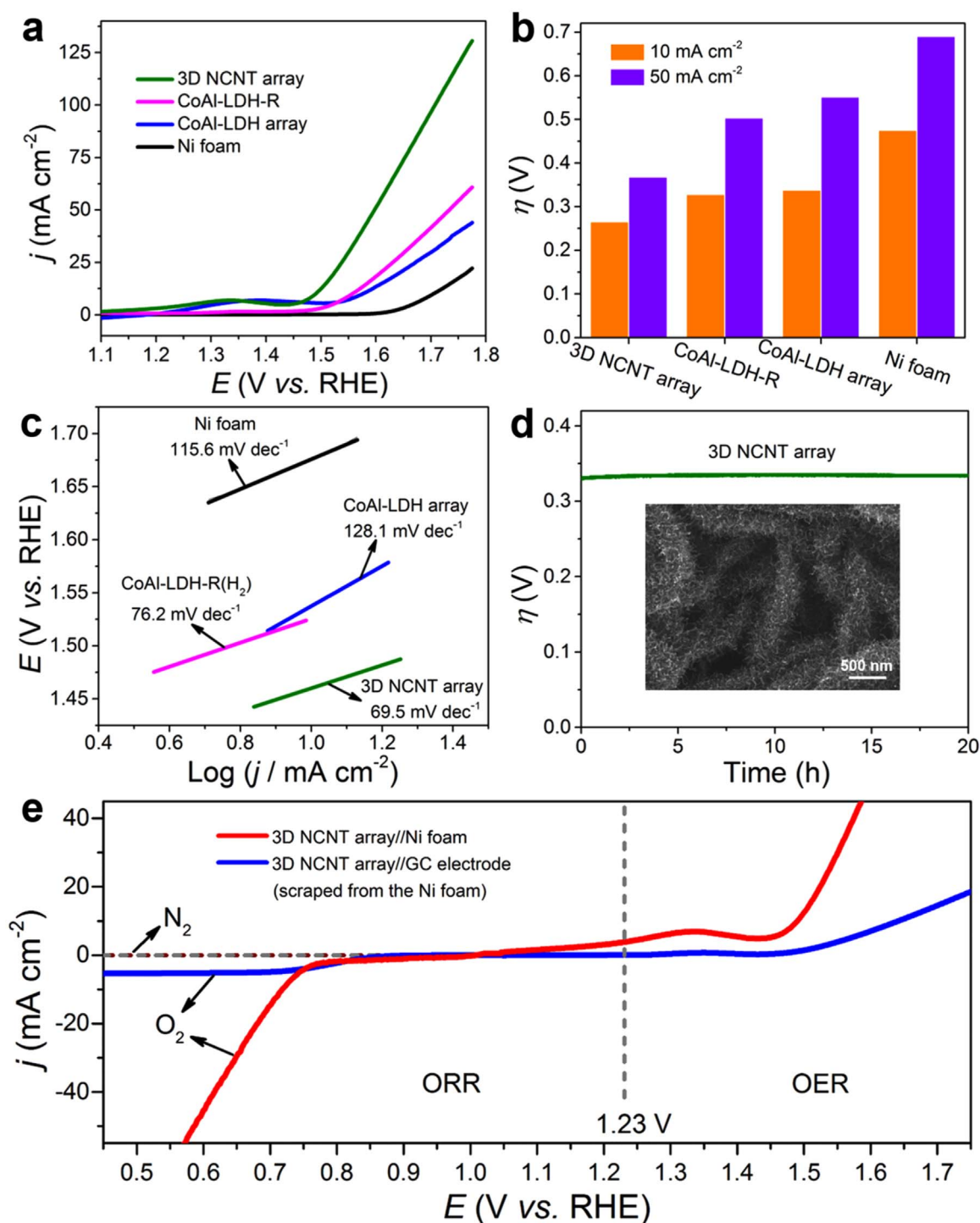


Fig. 5. Electrochemical oxygen evolution behavior over 3D NCNT array. (a) LSV curves of NCNT array and reference samples. (b) overpotential ($\eta_{j=10}$, $\eta_{j=50}$) and (c) Tafel plots for different catalysts derived from (a). (d) Chronopotentiometry measurements for the NCNT array at 10 mA cm⁻² for 20 h (inset: the corresponding SEM image of 3D NCNT array electrode after 20 h of OER test). (e) ORR and OER polarization curves for the NCNT array/Ni foam and NCNT/GC electrode, respectively.

shows the rate capability of the NCNT array at various galvanostatically discharged current density. The average voltage plateaus are 1.31, 1.26, 1.22, 1.13, and 1.01 V at the current densities of 2, 5, 10, 25, and 50 mA cm⁻², respectively, indicating a satisfactory rate capability. Furthermore, no obvious voltage drop was observed during the long-term galvanostatic discharge process (discharge for 16 h at 5 mA cm⁻²; Fig. S25), indicating an excellent durability. By normalized to the mass of consumed Zn, the NCNT array gives a specific capacity of

623.4 mAh g⁻¹, corresponding to an energy density of 776.5 Wh kg⁻¹. In addition, the battery cycling test was conducted to study the rechargeability of NCNT array. The Zn–air battery equipped with NCNT air-cathode shows stable and flat voltage platform in charging and discharging, with a charge/discharge potential of 1.98 V/1.23 V at 10 mA cm⁻² and 2.01 V/1.13 V at 25 mA cm⁻² (Fig. 6c). The calculated round-trip efficiency is 62% at 10 mA cm⁻², and remains 56% at 25 mA cm⁻², demonstrating the excellent bifunctional ORR/OER ac-

Table 1
Comparison of the electrocatalytic activities of the recently reported bifunctional catalysts for ORR/OER.

Catalyst	Electrolyte	$E_{1/2}$ vs. RHE (V)	$E_{j=10}$ vs. RHE (V)	ΔE (V) ($E_{j=10} - E_{1/2}$)	Ref
NCNF-1000	0.1 M KOH	0.82	1.84	1.02	[38]
Co ₃ N/CNW/CC	1 M KOH	0.8	1.54	0.74	[37]
Mn oxide	0.1 M KOH	0.73	1.77	1.04	[40]
ZnCo ₂ O ₄ /N-CNT	0.1 M KOH	0.87	1.65	0.78	[33]
NGM	0.1 M KOH	0.77	1.67	0.90	[9]
NGSH	0.1 M KOH	0.68	1.63	0.95	[42]
Mn _x O _y /NC	0.1 M KOH	0.81	1.68	0.87	[41]
Fe@N-C	0.1 M KOH	0.83	1.71	0.88	[43]
PCN-CFP	0.1 M KOH	0.67	1.63	0.96	[44]
Co ₂ O ₄ /CoMnO ₄	0.1 M KOH	0.68	1.77	1.09	[45]
NPMC-1000	0.1 M KOH	0.85	1.92	1.07	[1]
3D NCNT array	0.1 M KOH	0.81	1.65	0.84	This work

tivity of the electrocatalyst.

Light weight and flexible solid-state energy storage devices have attracted considerable attention for portable electronics [36]. Herein, a flexible all-solid-state Zn–air battery was fabricated by using zinc foil as the anode, NCNT array/Ni foam as air-cathode, and poly(vinyl alcohol) (PVA-KOH) as the solid electrolyte (Fig. 6d). The newly-developed all-solid-state Zn–air battery exhibits a stable discharge potentials (1.02 V) and charge potentials (1.98 V) at 5 mA cm⁻², even the device is bended to a large angle (Fig. 6e and Fig. S26). The specific capacity and energy density reach as high as 356 mAh g⁻¹ and

~382 Wh kg⁻¹, respectively, among the highest level of previously reported carbon-based catalysts [37–39]. Different from the air-electrodes prepared by conventional drop-casting method, the hierarchical NCNT structure provides sufficient electrocatalytic active sites and mass transport channels. For a metal–air battery, O₂ is necessary for the normal operation. Herein, the effect of atmosphere for the solid-state Zn–air battery was investigated by galvanostatic discharging measurements. As shown in Fig. 6f, a sharp voltage drop is observed without voltage output in N₂ atmosphere; when the battery is placed in the air or O₂ environment, a constant voltage output is obtained (1.02 V in air and 1.13 V in O₂ at a current density of 5 mA cm⁻²). Two series-connected all-solid-state Zn–air micro batteries can be used to power a red LED (Fig. 6f), indicating a potential application in flexible/wearable optoelectronic devices.

4. Conclusion

In summary, a well-defined 3D NCNT array has been successfully prepared *via* a directed growth method by using LDH as catalyst precursor and MOFs particles as carbon and nitrogen source. The resulting 3D NCNT array shows a hierarchical cactus-like morphology, uniform N-doping and low charge-transfer resistance, which exhibits excellent bifunctional ORR/OER electrocatalytic activity and stability. By virtue of the bifunctionality, the as-fabricated flexible all-solid-state Zn–air battery device (NCNT array//Zn foil) displays a desirable operational performance with a high discharge voltage of 1.02 V and low charge voltage of 1.98 V (at 5 mA cm⁻²), which is superior to most of the reported carbon-based catalysts. It is expected that the 3D NCNT array-based Zn–air battery can be potentially used in highly-efficient and stable energy storage devices.

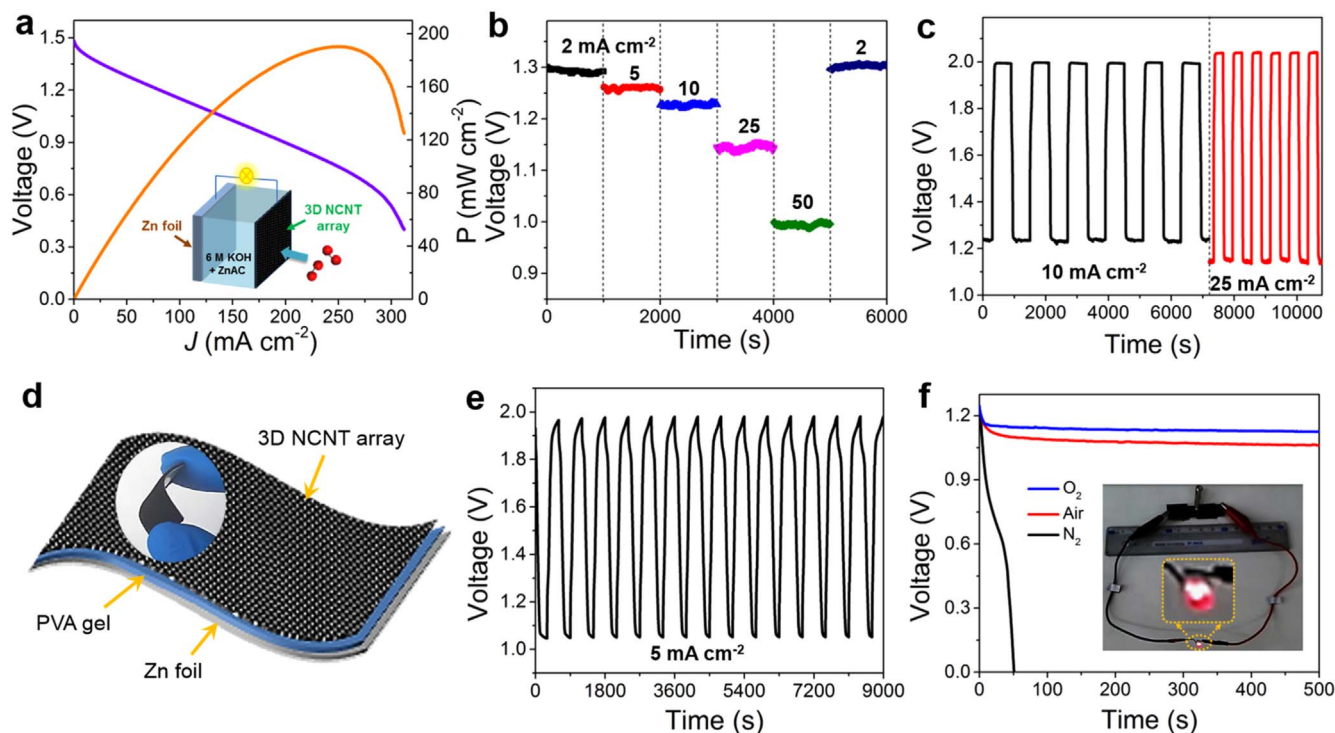


Fig. 6. Performances of NCNT array-based Zn–air battery. (a) Polarization curve and corresponding power density plot of the liquid Zn–air battery using NCNT array as cathode catalyst (inset: schematic illustration of the liquid Zn–air battery). (b) Galvanostatic discharge curves and (c) Galvanostatic discharge–charge cycling curves of the liquid Zn–air battery at different current densities. (d) Schematic representation and a photograph (inset) of the flexible all-solid-state Zn–air battery. (e) Galvanostatic discharge–charge curve for the as-prepared all-solid-state Zn–air battery. (f) Galvanostatic discharge curve for the flexible Zn–air battery in different atmosphere at 5 mA cm⁻² (inset: photograph of a red LED powered by two Zn–air micro batteries in series).

Acknowledgements

This work was supported by the National Natural Science Foundation of China (NSFC), the 973 Program (Grant No. 2014CB932102) and the Fundamental Research Funds for the Central Universities (buctrc201506; YS 1406). M. Wei particularly appreciates the financial aid from the China National Funds for Distinguished Young Scientists of the NSFC.

Appendix A. Supporting information

Supplementary data associated with this article can be found in the online version at doi:10.1016/j.nanoen.2017.05.016.

References

- [1] J. Zhang, Z. Zhao, Z. Xia, L. Dai, *Nat. Nanotechnol.* 10 (2015) 444–452.
- [2] Y. Li, M. Gong, Y. Liang, J. Feng, J.-E. Kim, H. Wang, G. Hong, B. Zhang, H. Dai, *Nat. Commun.* 4 (2013) 1805.
- [3] H. Wu, J. Wang, G. Wang, F. Cai, Y. Ye, Q. Jiang, S. Sun, S. Miao, X. Bao, *Nano Energy* 30 (2016) 801–809.
- [4] B.Y. Xia, Y. Yan, N. Li, H.B. Wu, X.W. Lou, X. Wang, *Nat. Energy* 1 (2016) 15006.
- [5] C. Tang, H. Wang, H. Wang, Q. Zhang, G. Tian, J. Nie, F. Wei, *Adv. Mater.* 27 (2015) 4516–4522.
- [6] G. Wu, A. Santandreu, W. Kellogg, S. Gupta, O. Ogoke, H. Zhang, H.-L. Wang, L. Dai, *Nano Energy* 29 (2016) 83–110.
- [7] S. Guo, X. Zhang, W. Zhu, K. He, D. Su, A. Mendoza-Garcia, S.F. Ho, G. Lu, S. Sun, *J. Am. Chem. Soc.* 136 (2014) 15026–15033.
- [8] Z.Y. Lu, H.T. Wang, D.S. Kong, K. Yan, P.C. Hsu, G.Y. Zheng, H.B. Yao, Z. Liang, X.M. Sun, Y. Cui, *Nat. Commun.* 5 (2014) 4345.
- [9] Y. Jiao, Y. Zheng, M. Jaroniec, S.Z. Qiao, *Chem. Soc. Rev.* 44 (2015) 2060–2086.
- [10] J. Zhang, L. Dai, *Angew. Chem. Int. Ed.* 128 (2016) 13490–13494.
- [11] M. Shao, Q. Chang, J.-P.P. Dodelet, R. Chenitz, *Chem. Rev.* 116 (2016) 3594–3657.
- [12] Z. Wang, Y. Lu, Y. Yan, T.Y.P. Larissa, X. Zhang, D. Wu, H. Zhang, Y. Yang, X. Wang, *Nano Energy* 30 (2016) 368–378.
- [13] G. Tian, Q. Zhang, B. Zhang, Y. Jin, J. Huang, D. Su, F. Wei, *Adv. Funct. Mater.* 24 (2014) 5956–5961.
- [14] G. Wu, K.L. More, C.M. Johnston, P. Zelenay, *Science* 332 (2011) 443–447.
- [15] J. Ziegelbauer, T. Olson, S. Pylypenko, F. Alamgir, C. Jaye, P. Atanassov, S. Mukerjee, *J. Phys. Chem. C* 112 (2008) 8839–8849.
- [16] N. Andersen, A. Serov, P. Atanassov, *Appl. Catal. B: Environ.* 163 (2015) 623–627.
- [17] J.P. Paraknowitsch, A. Thomas, *Energy Environ. Sci.* 6 (2013) 2839–2855.
- [18] S. Wang, E. Iyyamperumal, A. Roy, Y. Xue, D. Yu, L. Dai, *Angew. Chem. Int. Ed.* 50 (2011) 11756–11760.
- [19] K.P. Gong, F. Du, Z.H. Xia, M. Durstock, L.M. Dai, *Science* 323 (2009) 760–764.
- [20] K. Qu, Y. Zheng, S. Dai, S.Z. Qiao, *Nano Energy* 19 (2016) 373–381.
- [21] Z. Chen, C. Xu, C. Ma, W. Ren, H.-M. Cheng, *Adv. Mater.* 25 (2013) 1296–1300.
- [22] Y. Zhao, C. Hu, L. Song, L. Wang, G. Shi, L. Dai, L. Qu, *Energy Environ. Sci.* 7 (2014) 1913–1918.
- [23] X.C. Gui, J.Q. Wei, K.L. Wang, A.Y. Cao, H.W. Zhu, Y. Jia, Q.K. Shu, D.H. Wu, *Adv. Mater.* 22 (2010) 617–621.
- [24] S. Nardecchia, D. Carriazo, M.L. Ferrer, M.C. Gutiérrez, F. del Monte, *Chem. Soc. Rev.* 42 (2013) 794–830.
- [25] Z. Li, M. Shao, L. Zhou, R. Zhang, C. Zhang, M. Wei, D.G. Evans, X. Duan, *Adv. Mater.* 28 (2016) 2337–2344.
- [26] Y. Zhao, R. Nakamura, K. Kamiya, S. Nakanishi, K. Hashimoto, *Nat. Commun.* 4 (2013) 2390.
- [27] J. Sun, H. Liu, X. Chen, D. Evans, W. Yang, X. Duan, *Adv. Mater.* 25 (2013) 1125–1130.
- [28] J. Tang, R.R. Salunkhe, J. Liu, N.L. Torad, M. Imura, S. Furukawa, Y. Yamauchi, *J. Am. Chem. Soc.* 137 (2015) 1572–1580.
- [29] X.Z. Liao, A. Serquis, Q.X. Jia, D.E. Peterson, Y.T. Zhu, H.F. Xu, *Appl. Phys. Lett.* 82 (2003) 2694–2696.
- [30] M.F. Shao, R.K. Zhang, Z.H. Li, M. Wei, D.G. Evans, X. Duan, *Chem. Commun.* 51 (2015) 15880–15893.
- [31] Q. Wang, D. O'Hare, *Chem. Rev.* 112 (2012) 4124–4155.
- [32] X. Lu, W.-L. Yim, B.H. Suryanto, C. Zhao, *J. Am. Chem. Soc.* 137 (2015) 2901–2907.
- [33] H.X. Zhong, J. Wang, Y.W. Zhang, W.L. Xu, W. Xing, D. Xu, Y.F. Zhang, X.B. Zhang, *Angew. Chem. Int. Ed.* 53 (2014) 14235–14239.
- [34] Z.Q. Liu, H. Cheng, N. Li, T.Y. Ma, Y.Z. Su, *Adv. Mater.* 28 (2016) 3777–3784.
- [35] Y. Li, H. Dai, *Chem. Soc. Rev.* 43 (2014) 5257–5275.

- [36] A. Sekiguchi, F. Tanaka, T. Saito, Y. Kuwahara, S. Sakurai, D.N. Futaba, T. Yamada, K. Hata, *Nano Lett.* 15 (2015) 5716–5723.
- [37] F. Meng, H. Zhong, D. Bao, J. Yan, X. Zhang, *J. Am. Chem. Soc.* 138 (2016) 10226–10231.
- [38] Q. Liu, Y. Wang, L. Dai, J. Yao, *Adv. Mater.* 28 (2016) 3000–3006.
- [39] D.U. Lee, J.Y. Choi, K. Feng, H.W. Park, Z.W. Chen, *Adv. Energy Mater.* 4 (2014) 1301089.
- [40] Y. Gorlin, T.F. Jaramillo, *J. Am. Chem. Soc.* 132 (2010) 13612–13614.
- [41] G.L. Tian, M.Q. Zhao, D. Yu, X.Y. Kong, J.Q. Huang, Q. Zhang, F. Wei, *Small* 10 (2014) 2251–2259.
- [42] J. Masa, W. Xia, I. Sinev, A. Zhao, Z. Sun, S. Grütze, P. Weide, M. Muhler, W. Schuhmann, *Angew. Chem. Int. Ed.* 53 (2014) 8508–8512.
- [43] J. Wang, H. Wu, D. Gao, S. Miao, G. Wang, X. Bao, *Nano Energy* 13 (2015) 387–396.
- [44] T.Y. Ma, J. Ran, S. Dai, M. Jaroniec, S.Z. Qiao, *Angew. Chem. Int. Ed.* 54 (2015) 4646–4650.
- [45] D. Wang, X. Chen, D.G. Evans, W. Yang, *Nanoscale* 5 (2013) 5312–5315.



Zhenhua Li received his Bachelor's degree from Beijing University of Chemical Technology (BUCT) in Polymer Science and engineering in 2014. He is now a Ph.D. candidate under the supervision of Prof. Xue Duan in the BUCT. His research interests mainly focus on the synthesis of nanostructured layered double hydroxides and their application in the energy storage and conversion.



Mingfei Shao received his PhD degree from Beijing University of Chemical Technology in 2014, after which he joined the staff of BUCT. He was also a visiting student at the University of Oxford in 2013. His current research interests are mainly focused on the controlled synthesis of layered functional materials and their applications in electrochemical and photoelectrochemical energy storage and conversions.



Qihui Yang received her Bachelor's degree in 2015 from Henan University of Technology. She is now a post-graduate under the supervision of Dr. Mingfei Shao in Beijing University of Chemical Technology (BUCT). Her research interests currently focus on the fabrication of electrode materials for energy storage.



Yang Tang received his PhD degree from Beijing University of Chemical Technology (BUCT) in 2013 under the supervision of Prof. Pingyu Wan, after which he continued working as a staff in BUCT. His research interests focus on the design and fabrication of nanomaterials for electrochemical and catalytic applications such as PEM fuel cell, direct methanol and formic acid fuel cells, energy-saving electrolysis, and supercapacitors.



Min Wei obtained her BEng degree in 1995 and MEng degree in 1998 from Beijing University of Chemical Technology (BUCT). She subsequently received her PhD from Peking University in 2001, after which she joined the staff of BUCT. She was promoted to full Professor in 2005. She has been a visiting scholar in the Georgia Institute of Technology (in 2008). Her research interests focus on inorganic-organic composite functional materials as well as new catalysts.



Xue Duan was elected as an Academician of the Chinese Academy of Sciences in 2007. He was awarded his BS degree from Jilin University and MS and PhD degrees from Beijing University of Chemical Technology (BUCT). He was subsequently appointed to the staff of BUCT and established the Applied Chemistry Research Institute in 1990. He was promoted to full Professor in 1993 and to PhD supervisor status in 1995. He is currently Director of the Institute of Applied Chemistry and Executive Vice-Chair of the Academic Committee of the State Key Laboratory of Chemical Resource Engineering.



David G. Evans studied as both an undergraduate and a research student at Jesus College, Oxford, and obtained a DPhil under the supervision of Prof. D. M. P. Mingos FRS. After postdoctoral work at Bristol University with Prof. F. G. A. Stone FRS, he was appointed as a lecturer at Exeter University in 1985. Several visits to Chinese university chemistry departments in the early 1990s convinced him of China's great potential for development and he moved to Beijing University of Chemical Technology in 1996. His research interests focus on intercalation in layered solids.